Front. Mater. Sci. 2018, 12(3): 247–263
https://doi.org/10.1007/s11706-018-0433-0

RESEARCH ARTICLE

Synthesis of $BaWO_4$/NRGO–g-C_3N_4 nanocomposites with excellent multifunctional catalytic performance via microwave approach

M. Mohamed Jaffer SADIQ[1], U. Sandhya SHENOY[2], and D. Krishna BHAT (✉)[1]

1 Department of Chemistry, National Institute of Technology Karnataka Surathkal, Mangalore-575025, India
2 Department of Chemistry, College of Engineering and Technology, Srinivas University, Mukka, Mangalore-574146, India

ABSTRACT: Novel barium tungstate/nitrogen-doped reduced graphene oxide–graphitic carbon nitride ($BaWO_4$/NRGO–g-C_3N_4) nanocomposite has been synthesized by a simple one-pot microwave technique. The synthesized nanocomposites are well characterized by diffraction, microscopic and spectroscopic techniques to study its crystal structure, elemental composition, morphological features and optical properties. The material prepared is tested for its performance as an electrocatalyst, photocatalyst and reduction catalyst. The nanocomposite catalyzed the photodegradation of methylene blue (MB) dye in 120 min, reduction of 4-nitro phenol (4-NP) to 4-amino phenol (4-AP) in 60 s, showed an impressive Tafel slope of 62 mV/dec for hydrogen evolution reaction (HER). The observed results suggest that the nanocomposite acts as an efficient multifunctional catalyst. The reported approach provides fundamental insights which can be extended to other metal tungstate-based ternary composites for applications in the field of clean energy and environment in the future.

KEYWORDS: $BaWO_4$/NRGO–g-C_3N_4 nanocomposites; microwave irradiation; hydrogen evolution reaction; photocatalyst; reduction

Contents

Received May 13, 2018; accepted June 25, 2018

E-mail: denthajekb@gmail.com

1 Introduction

The abundance of existing major sources of energy such as coal, natural gas and other fossil fuels is limited and they are non-renewable too. With increase in the population, the global energy demand has increased and society is not able to cope with the demand. The quest for renewable clean energy sources has turned our attention towards hydrogen [1]. Hydrogen can be produced by water splitting through electrocatalysis. But most of the materials currently used for electrocatalytic water splitting are noble and expensive. Development of low cost and environmental friendly electrocatalyst is the need of the day now to commercialize hydrogen production [2]. Semiconductor photocatalysis has attracted interest of research community as it can solve both environmental and energy problems [2–3]. A good photocatalyst should have an extended excitation wavelength, low recombination rate of charge carriers and active sites on the surface to facilitate adsorption and reaction. Several strategies have been developed to achieve the above said properties like doping, coupling with semiconductors and compositing with layered materials to improve the surface area [3]. Despite these efforts, commercialization of these materials is yet to be realized. Hence, designing of materials with multifaceted catalytical activity such as, high performance towards electrolysis, photodegradation and reduction, which would help in solving the energy and environmental problems, must be thoroughly considered. Such multifunctional catalysts will provide an economic way to serve several applications.

Graphene-based architectures not only provide support to other materials but also have a potential to harness the electrical and redox properties [4–6]. The electronic property and the chemical reactivity of graphene can be tailored by doping nitrogen [7–8]. In N-doped graphene ~0.5 electron per N atom is provided to carbon π conjugated system thus enhancing the photocatalytic efficiency. When composited with semiconductors, nitrogen-doped reduced graphene oxide (NRGO) increases the rate of transfer of electrons from the conduction band of semiconductors in comparison with graphene.

Graphitic carbon nitride (g-C_3N_4), a metal-free polymeric semiconductor with higher nitrogen content and porous structure, has attracted significant attentions in the field of photocatalysis due to its good thermal-chemical stability, electronic and optical characteristics, low cost and non-toxicity. g-C_3N_4 possesses a bandgap of ~2.7 eV with the conduction band (CB) position at − 1.1 eV and valence band (VB) position at + 1.6 eV. As the CB potential of g-C_3N_4 is sufficiently negative, the strong reducing capability of electrons in the CB of g-C_3N_4 surface can have great potential for photocatalytic studies [9–11]. Combining g-C_3N_4 with other appropriate semiconductors to form semiconductor heterostructure is considered as an effective method to enhance photocatalytic activity.

Semiconducting materials which possess narrow bandgap have been used as photocatalysts, as their bandgap energy lies in the energy range of ultraviolet (UV) or visible light [12–13]. Tungsten oxides, hydrates and metal tungstates have been studied for their photocatalytic capabilities [14–15]. In particular, $ZnWO_4$, $CoWO_4$, $FeWO_4$ and $NiWO_4$ have been extensively used for preparation of composites for water splitting [16–19]. On the other hand, $BaWO_4$ which has a wide variety of applications has been studied meagerly in the field of photocatalysis due to its instability and slow electron transfer rate. To extend the absorption of $BaWO_4$ from the UV region to the visible-light region of solar spectrum the bandgap should be decreased. Since smaller bandgap leads to higher recombination rate, the transport property is tuned by doping carbon-based material to improve the photocatalytic efficiency [20].

It is well known that use of the microwave irradiation over conventional heating has obvious advantages such as, uniform and volumetric heating, short reaction time and uniformity in the size and shape of formed nanoparticles without much need of high temperature and pressure. Several reports are available in support of the advantages of microwave assisted approach over conventional methods for the synthesis of nanocomposites [16–20].

Based on the above facts, we report here the synthesis of $BaWO_4$/NRGO–g-C_3N_4 nanocomposites via a facile, simple one-pot microwave method. To the best of our knowledge this is the first report on such kind of ternary nanocomposite with tri-functional utility. The as-synthesized material is thoroughly characterized using various advanced techniques. The reported material is highly efficient in catalyzing hydrogen evolution reaction (HER), degradation of methylene blue (MB) dye and reduction of 4-nitro phenol (4-NP) to 4-amino phenol (4-

AP). The reported approach is extendible to other metal tungstate nanocomposites as well.

2 Experimental

2.1 Materials

All the reagents and chemicals were of analytical grade and used without further purification. Deionized water was used throughout the study.

2.2 Synthesis of $BaWO_4$

$BaWO_4$ nanoparticles were prepared by a simple microwave route. In a typical synthesis, solutions of barium chloride, ammonium tungstate and cetyltrimethyl ammonium bromide (CTAB) in H_2O/ethanol were prepared with desired molar ratio and mixed together using ultrasonication for about 30 min. The resulting mixture was treated with microwave irradiation at 350 W for 10 min and then allowed to cool to room temperature. The obtained precipitate of $BaWO_4$ was filtered and washed thoroughly with 10% ethanol several times to remove the impurities. Finally, the precipitate was dried at 60°C overnight.

2.3 Synthesis of graphene oxide (GO)

GO was prepared through chemical exfoliation of natural graphite powder by a modified Hummers' method previously reported [21]. 5 g of graphite flakes and 2.5 g of $NaNO_3$ was added in 150 mL of concentrated H_2SO_4 under constant stirring in a beaker immersed in an ice water bath. Then, 15 g of $KMnO_4$ was added slowly and the mixture was stirred at the 30°C for 2 h and then for 30 min at 95°C. Finally, the reaction mixture was diluted with distilled water and 10 mL of H_2O_2 was subsequently added. The GO obtained was separated from the yellow solution by centrifugation, washed with dilute HCl and water until the pH was 7. Later it was exfoliated by sonication.

2.4 Synthesis of g-C_3N_4

The powder of g-C_3N_4 was prepared according to the previously reported technique [22]. Typically, 2 g of melamine was put into a semi-closed alumina crucible which was calcined at 550°C with a heating rate of 10°C/min for 4 h in the air atmosphere in a muffle furnace. The obtained light-yellow g-C_3N_4 product was collected and ground into powder form, then thoroughly washed with deionized water, and dried at 60°C overnight for further use.

2.5 Synthesis of $BaWO_4$/NRGO–g-C_3N_4 nanocomposites

$BaWO_4$/NRGO(A)–g-C_3N_4(B) nanocomposites (A = 2.5 wt.% GO; B = 5%, 10% and 20% of g-C_3N_4) were prepared using a simple microwave route. In a typical synthesis, a well-mixed solution of (0.01 mol/L) barium chloride, (0.01 mol/L) ammonium tungstate, (0.1%) CTAB and (1.0 g) urea in 50 mL of H_2O/ethanol was prepared. To this, a solution containing calculated amounts of GO(A) and g-C_3N_4(B) dispersed in water was added under constant stirring. The pH of the reaction mixture was maintained at 9 using ammonia. After 30 min of ultrasonication, the resulting mixture was treated with microwave irradiation at 350 W for 10 min and then allowed to cool to room temperature. The obtained precipitate of $BaWO_4$/NRGO–g-C_3N_4 nanocomposite was filtered and washed thoroughly with 10% ethanol several times and finally dried at 60°C overnight.

Similarly, $BaWO_4$/g-C_3N_4 and $BaWO_4$/NRGO nanocomposites were prepared using appropriate starting materials. $BaWO_4$/NRGO nanocomposites with the NRGO content varying from 0.5% to 5% were prepared and their catalytic efficiency for photodegradation of MB dye was tested. The nanocomposite with 2.5% NRGO showed the highest activity and hence 2.5% NRGO was taken as the optimized composition for $BaWO_4$/NRGO nanocomposites. Similarly, in the case of $BaWO_4$/NRGO–g-C_3N_4 ternary nanocomposites, keeping the NRGO content fixed at 2.5%, the g-C_3N_4 content was varied from 5% to 20%. The nanocomposite with 10% g-C_3N_4 showed the maximum catalytic activity and hence it was taken as the optimized composition of g-C_3N_4 in the ternary nanocomposite (Fig. S1). Schematic representation of the synthesis of $BaWO_4$/NRGO–g-C_3N_4 nanocomposites is shown in Fig. S2.

2.6 Characterization

The powder X-ray diffraction (XRD) patterns were recorded using X-ray diffractometer (Rigaku, Japan) with the Cu Kα target (λ = 0.15406 nm) in the 2θ range 5° to 80° with a scan rate of 1(°)/min. The specific surface area was obtained using SMART SORB 92/93 (Smart Instruments Company Private Limited) by the Brunauer–Emmett–Teller (BET) method. The surface morphology was

obtained using scanning electron microscopy (SEM, JEOL) and high-resolution transmission electron microscopy (HRTEM, Technai). Laser Raman microscope (RenishawInvia) was used to obtain Raman spectrum using excitation laser wavelength source of 532 nm. X-ray photoelectron spectroscopy (XPS) was done to determine the chemical states of the samples with Multilab2000 (ThermoScientific, UK) and the obtained data was calibrated using contaminant carbon at a binding energy of 284.8 eV. UV-visible diffuse reflectance data were collected with a spectrophotometer (Analytik Jena). Photoluminescence (PL) spectra were obtained using Horiba JobinYvon spectrometer with excitation wavelength of 380 nm. The total organic carbon concentration (TOC) was measured using total organic carbon analyzer (TOC-V CSN, Shimadzu, Japan).

2.7 Photocatalytic measurements

The photocatalytic activity of $BaWO_4$/NRGO–g-C_3N_4 nanocomposites in the degradation of MB was evaluated as follows. Firstly, 0.02 g of $BaWO_4$/NRGO–g-C_3N_4 nanocomposite was dispersed into a 200 mL MB (10 mg/L) aqueous solution in a Pyrex glass vessel and then the dispersion was kept in the dark for 30 min at room temperature to establish the adsorption equilibrium. The solution was irradiated using an Hg lamp (250 W with 400 nm cutoff filter). During the irradiation, samples were taken out at given time intervals, filtered and then the concentration of MB was determined at 664 nm using a UV-visible spectrophotometer (Analytik Jena) from which percentage degradation was calculated. For comparison, the photocatalytic activities of the components of the composite were also tested following the same procedure. In the recycling experiment, the catalysts were collected and washed several times with 10% ethanol, before the next cycle.

To identify the nature of degradation process, the extent of mineralization of the dye during the photodegradation was estimated. The mineralization of the dye was calculated by using the TOC analysis. The TOC was analyzed before the start of the experiment (TOC_0) and at specified intervals during the photodegradation reaction (TOC_t). The mineralization percentage of MB dye (σ_{MB}) was calculated by using the following equation:

$$\sigma_{MB}/\% = \frac{TOC_0 - TOC_t}{TOC_0} \times 100 \quad (1)$$

where, TOC_0 is the initial concentration and TOC_t is the concentration at a given interval time, of the MB dye solution, respectively.

In addition, to determine the mechanism of the photocatalytic activity, experiments were carried out using various radical scavengers like t-BuOH (TBA, 10 mmol/L), KI (potassium iodide, 10 mmol/L), BQ (benzoquinone, 1 mmol/L) and $AgNO_3$ (silver nitrate, 10 mmol/L) which acted as the scavengers for hydroxyl radicals (•OH), holes (h^+), superoxide radicals ($\bullet O_2^-$) and electrons (e^-), respectively as reported previously [23].

2.8 Reduction

The reduction of 4-NP to 4-AP by using $NaBH_4$ at ambient temperature was chosen as a model reaction to test the catalytic activity of the $BaWO_4$/NRGO–g-C_3N_4 nanocomposites. 0.3 mL of freshly prepared $NaBH_4$ solution (0.1 mol/L) was mixed with 2.7 mL of an aqueous 4-NP solution (0.1 mmol/L) in a quartz cuvette, leading to an immediate color change from light yellow to yellow-green. Then, 0.0005 g of $BaWO_4$/NRGO–g-C_3N_4 nanocomposites was added to start the reduction reaction and the reaction progress was monitored at 400 nm by using UV-visible spectroscopy (Analytik Jena) at a regular time interval of 15 s. For comparison, the catalytic activities of components of the composite were also tested following the same procedure. In the recycling experiment, the catalysts were collected and washed several times with 10% ethanol and then reused.

2.9 Electrocatalytic measurements

All electrochemical measurements were performed using an IVIUM potentiostat in a conventional three-electrode cell. A glassy carbon disk with a geometric area of 0.07065 cm^2 modified with the catalysts was used as the working electrode, an Ag/AgCl (3 mol/L KCl) as a reference electrode and a Pt wire as the counter electrode were employed for electrochemical measurements. 0.1 mol/L KOH solution was used as the electrolyte. The reference electrode was calibrated with respect to the reversible hydrogen electrode (RHE). Prior to experiments, the glassy carbon electrode was polished with a polishing cloth using different alumina pastes (3.0–0.05 mm) to obtain a mirror-like surface, followed by ultrasonic cleaning in water. For electrochemical measurements, a catalyst ink was prepared by dispersing 2.0 mg/mL of the catalyst in water that contained 0.1 wt.% Nafion under ultrasonication for 30 min. 5.0 μL of the catalyst suspension was drop-coated

onto the polished glassy carbon electrode and dried in air at room temperature. Linear sweep voltammetry (LSV) was done at a scan rate of 10 mV/s to evaluate the HER performance of the working electrode. The long-term stability was evaluated by chronopotentiometry at a current density of -10 mA/cm^2 using a glassy carbon disk (3 mm diameter) modified with the catalyst. The catalyst loading for each electrode was 0.142 mg/cm^2. All the measurements were carried out at room temperature. Also, before the experiment, electrolyte solution was purged with N_2 for 30 min to remove the oxygen completely.

3 Results and discussion

3.1 XRD studies

The XRD patterns of NRGO, g-C_3N_4, $BaWO_4$, $BaWO_4$/NRGO and $BaWO_4$/NRGO–g-C_3N_4 nanocomposites are shown in Fig. 1. The diffraction peak at 2θ = 24.4° corresponds to the (002) reflection plane of reduced phase of NRGO. The peaks at 2θ = 12.8° and 27.5° seen in pure g-C_3N_4 can be indexed to the (100) and the (002) diffraction planes conforming to the JCPDS No. 87-1526 of the graphitic carbon nitride. The diffraction pattern of $BaWO_4$ matches well with JCPDS No. 43-0646 suggesting that the material has the scheelite-type tetragonal crystal structure with the space group of the I41/a symmetry [24]. The peaks found at 2θ values 17.3°, 26.5°, 28.1°, 31.9°, 43.0°, 45.7°, 48.7°, 53.6°, 54.5°, 66.6°, 67.7°, 69.4°, 73.0°, 73.8°, 75.8° and 76.8° can be ascribed to the (101), (112), (004), (200), (204), (220), (116), (312), (224), (400), (208), (411), (332), (404), (420) and (228) planes of $BaWO_4$. $BaWO_4$/NRGO and $BaWO_4$/NRGO–g-C_3N_4 nanocomposite have similar diffraction peaks corresponding to $BaWO_4$. These results specify that the introduction of NRGO and NRGO–g-C_3N_4 does not disturb the orientation and structure of scheelite $BaWO_4$.

3.2 Raman studies

The as-synthesized nanocomposites are further characterized by using Raman spectroscopy. As shown in Fig. 2, five peaks are exhibited at 334, 478, 794, 830 and 927 cm^{-1} in the pure $BaWO_4$ sample. The bands positioned around 334 cm^{-1} is indexed to the stretching vibration of the BaO_6 octahedra. The bands located at 478, 794 and 830 cm^{-1} are assigned to the W – O stretching vibration of the WO_4 tetrahedra. The band at 927 cm^{-1} is associated with the WO_6 symmetric stretching vibration of the crystalline $BaWO_4$ [25]. The Raman spectrum of the pure NRGO reveals two prominent peaks of D band and G band at 1356 and 1598 cm^{-1}, respectively [7–8]. The Raman spectrum of the $BaWO_4$/NRGO–g-C_3N_4 nanocomposites contains all the bands corresponding to $BaWO_4$ and NRGO. The ratios of I_D/I_G in pure NRGO and $BaWO_4$/NRGO–g-C_3N_4 nanocomposites are 1.09 and 1.13, respectively. The higher value for ternary composite may be due to the interaction of NRGO, g-C_3N_4 and $BaWO_4$ leading to more defects and disorders in the $BaWO_4$/NRGO–g-C_3N_4 nanocomposite. The typical bands of g-C_3N_4 appear at 421, 605, 897, 1087, 1219 and 1339 cm^{-1} [10]. However, these bands of g-C_3N_4 are difficult to identify in the Raman spectrum of the $BaWO_4$/NRGO–g-C_3N_4 nanocomposite. This may be due to the weak scattering ability of g-C_3N_4 on the surface of the nanocomposite [10].

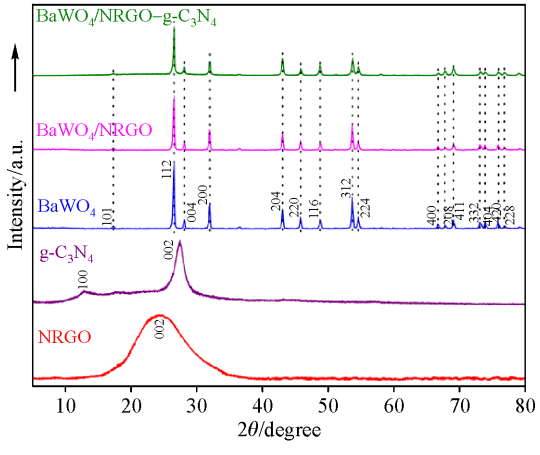

Fig. 1 XRD patterns of NRGO, g-C_3N_4, $BaWO_4$, $BaWO_4$/NRGO and $BaWO_4$/NRGO–g-C_3N_4 nanocomposites.

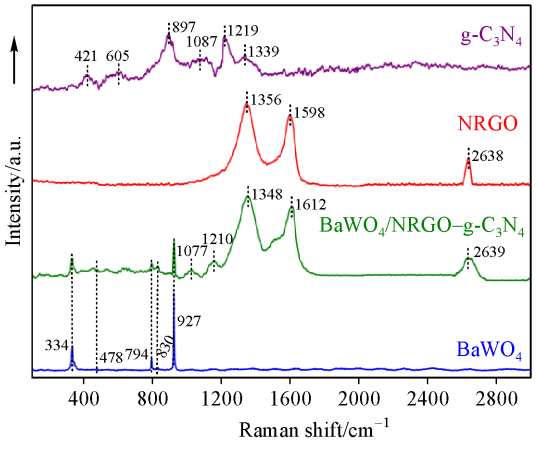

Fig. 2 Raman spectra of NRGO, g-C_3N_4, $BaWO_4$ and $BaWO_4$/NRGO–g-C_3N_4 nanocomposites.

3.3 FTIR studies

The presence of $BaWO_4$, NRGO and g-C_3N_4 in the as-synthesized nanocomposite can be identified using Fourier transform infrared spectroscopy (FTIR). As shown in Fig. 3, the main peak at 819 cm^{-1}, assigned to the stretching vibration of Ba – O, W – O and W – O – W, is seen in the spectrum of pure $BaWO_4$ and $BaWO_4$/NRGO–g-C_3N_4 nanocomposites [26]. As shown in the inset of Fig. 3, the peaks at 3406, 2969, 2884, 1633, 1465 and 1248 cm^{-1} in the FTIR spectra of NRGO and $BaWO_4$/NRGO–g-C_3N_4 nanocomposites can be ascribed to the asymmetric and symmetric vibrations of O – H and C – H, respectively [27]. The spectrum of g-C_3N_4 shows peaks at 1248, 1326, 1415, 1465, 1575 and 1633 cm^{-1} which are characteristic stretching modes of C – N heterocycles. The peaks at 808 and 3184 cm^{-1} are attributed to the typical breathing mode of triazine units and the stretching mode of N – H in g-C_3N_4, respectively [27]. The FTIR spectrum of $BaWO_4$/NRGO–g-C_3N_4 nanocomposites reveals similar peaks as that of g-C_3N_4. All the peaks corresponding to $BaWO_4$, NRGO and g-C_3N_4 are present in the spectrum of $BaWO_4$/NRGO–g-C_3N_4 nanocomposites.

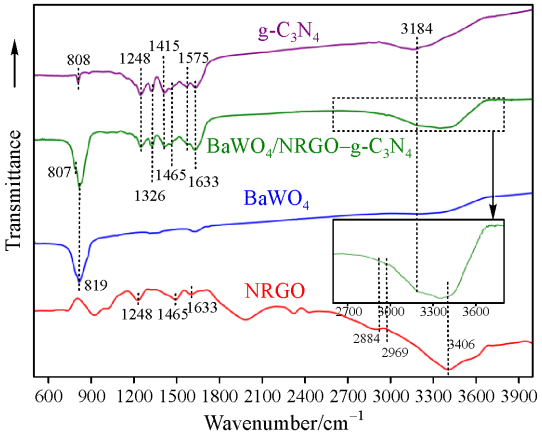

Fig. 3 FTIR spectra of NRGO, g-C_3N_4, $BaWO_4$ and $BaWO_4$/NRGO–g-C_3N_4 nanocomposites.

3.4 Surface morphology studies

The specific surface area of the as-synthesized nanocomposites was measured by the BET analysis. The specific surface areas of $BaWO_4$ and $BaWO_4$/NRGO–g-C_3N_4 nanocomposites are 3.51 and 25.02 m^2/g, respectively. It is very clear that the specific surface area increases due to the introduction of the NRGO and g-C_3N_4 on the $BaWO_4$ substrate. This increase in surface area facilitates the surface adsorption and creates more number of active sites resulting in enhanced catalytic activities [16].

The high-resolution transmission electron microscopy (HRTEM) image (Fig. 4(a)) reveals that $BaWO_4$ particles are successfully deposited on the surface of g-C_3N_4 and NRGO nanosheets. The spacing of the lattice fringes in the $BaWO_4$ is about 0.51 nm which corresponds to the (101) plane of scheelite-type tetragonal crystal phase (JCPDS No. 43-0646). In addition, the lattice spacing of about 0.34 nm corresponds to the (002) plane of the graphitic carbon nitride (JCPDS No. 87-1526) and lattice spacing of 0.36 nm corresponds to the (002) planes of the NRGO nanosheets. The selected area electron diffraction (SAED) pattern of the nanocomposite (inset of Fig. 4(a)) shows ring pattern indicating the polycrystalline nature of the sample. The particle size distribution of $BaWO_4$ (Fig. 4 (b)) shows that the average particle sizes is around 12 nm.

The EDX analysis (Fig. 4(c)) of $BaWO_4$/NRGO–g-C_3N_4 nanocomposites further compliments the characterization and formation of the ternary composite. In addition to that, the distribution of elements in $BaWO_4$/NRGO–g-C_3N_4 nanocomposites was determined by the elemental mapping analysis (Figs. 4(d)–4(h)). The analysis infers the uniform distribution of the particles in the composite.

3.5 XPS studies

XPS is used to investigate the elemental composition as well as the chemical environment on the surface of the as-prepared nanocomposites. XPS survey spectrum of $BaWO_4$/NRGO–g-C_3N_4 nanocomposites is shown in Fig. 5(a). The elemental peaks of C, N, O, Ba and W are found in the $BaWO_4$/NRGO–g-C_3N_4 nanocomposites, which confirm the presence of NRGO, g-C_3N_4, and $BaWO_4$ in the nanocomposite. High-resolution C 1s spectra (Fig. 5 (b)) can be deconvoluted into four peaks. Peaks at 284.2 and 285.3 eV can be allocated to carbon (C = C) and typical sp^2 carbon atoms bonded to N atoms in an aromatic ring (N – C = N), peak at 286.98 eV can be ascribed to C = N originated from NRGO and the formation of C – O – C bond between NRGO and g-C_3N_4 during microwave treatment. The peak at 288.03 eV can be ascribed to the interaction of C – N – C between g-C_3N_4 and NRGO. As shown in Fig. 5(c), five deconvoluted peaks in the high-resolution N 1s spectrum of $BaWO_4$/NRGO–g-C_3N_4 nanocomposites are assigned to pristine g-C_3N_4 (396.8 eV), pyridinic N (397.9 eV), pyrrolic N (399.1 eV), graphitic N (400.8 eV) and terminal amino groups (403.9

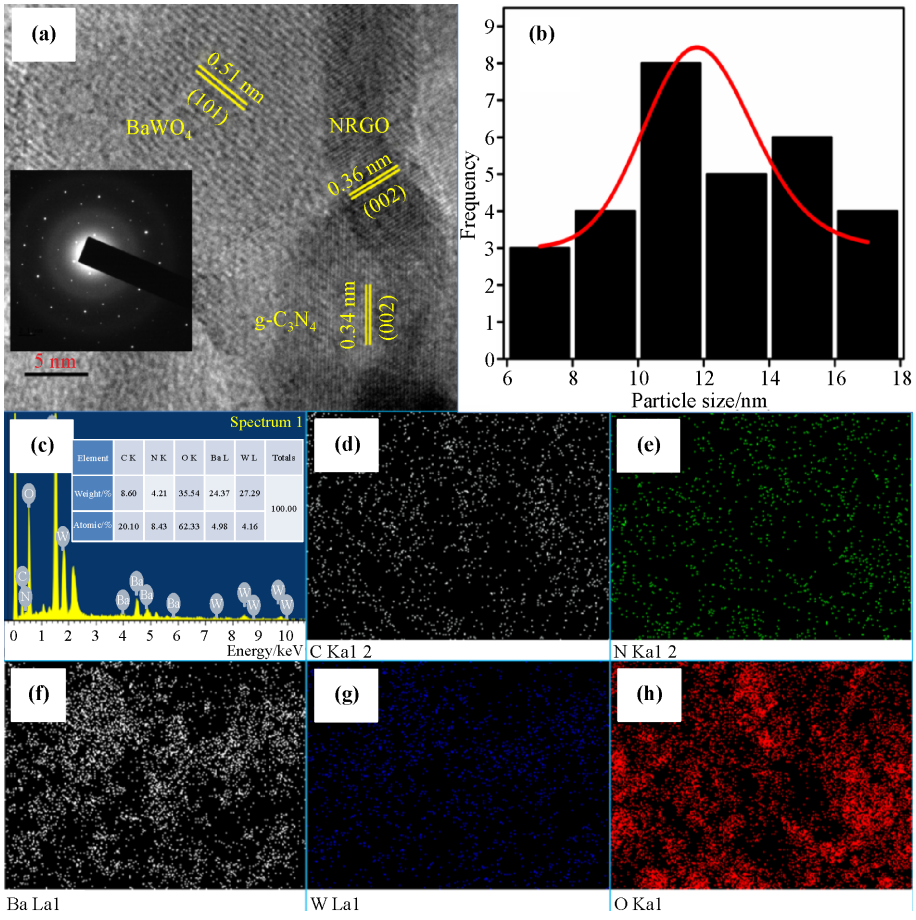

Fig. 4 **(a)** HRTEM image (inset showing SAED pattern), **(b)** particle size distribution, **(c)** EDX spectrum, and elemental mappings of **(d)** C, **(e)** N, **(f)** Ba, **(g)** W and **(h)** O of the $BaWO_4$/NRGO–g-C_3N_4 nanocomposites.

eV), which is in agreement with the reported data [9]. The O 1s peaks in Fig. 5(d) at 528.96, 530.48 and 534.03 eV correspond respectively to Ba – O – W, N – C – O and N – C – O – W of the $BaWO_4$/NRGO–g-C_3N_4 nanocomposites, revealing the chemical interaction between NRGO, g-C_3N_4 and $BaWO_4$ in the nanocomposites. As shown in Fig. 5(e), the doublet peaks at 37.1 and 35.0 eV belong to W $4f_{5/2}$ and W $4f_{7/2}$, respectively, which are the features of W^{6+} in pure $BaWO_4$ [20]. The peaks at 794.6 and 779.2 eV correspond to Ba $3d_{3/2}$ and Ba $3d_{5/2}$ (Fig. 5(f)), which can be assigned to Ba^{2+} of pure $BaWO_4$.

For comparison, survey and high-resolution XPS spectra of the as-synthesized NRGO is given in Fig. S3. XPS can be used to provide direct evidence for doping of N into RGO. The presence of N could be clearly detected in the XPS spectra of NRGO, and the high-resolution N 1s XPS spectra could be fitted into four types of N doping, including pyridinic N (398.3 eV), pyrrolic N (399.6 eV), graphitic N (400.7 eV) and pyridinic N oxide (402.5 eV). All the above results show that the N-doped RGO has been successfully synthesized. Further, the small differences in the binding energies observed for neat NRGO and NRGO in the nanocomposite can be attributed to the interactions of NRGO with other components of the composite.

3.6 Optical studies

The optical properties of NRGO, g-C_3N_4, $BaWO_4$, $BaWO_4$/NRGO and $BaWO_4$/NRGO–g-C_3N_4 nanocomposite are determined via the UV-visible diffuse reflectance spectroscopy (DRS) (Fig. 6(a)). As shown in Fig. 6(a), NRGO absorbs in the whole visible-light region. The $BaWO_4$/NRGO and $BaWO_4$/NRGO–g-C_3N_4 nanocomposites show higher absorption as well as wider wavelength window of absorption in the visible-light region compared with pure g-C_3N_4 and $BaWO_4$. Thus, the observation suggests that the $BaWO_4$/NRGO–g-C_3N_4 nanocomposite can efficiently utilize visible-light and generate more electron–hole pairs under visible-light irradiation.

For a given semiconductor, its bandgap energy (E_g) can

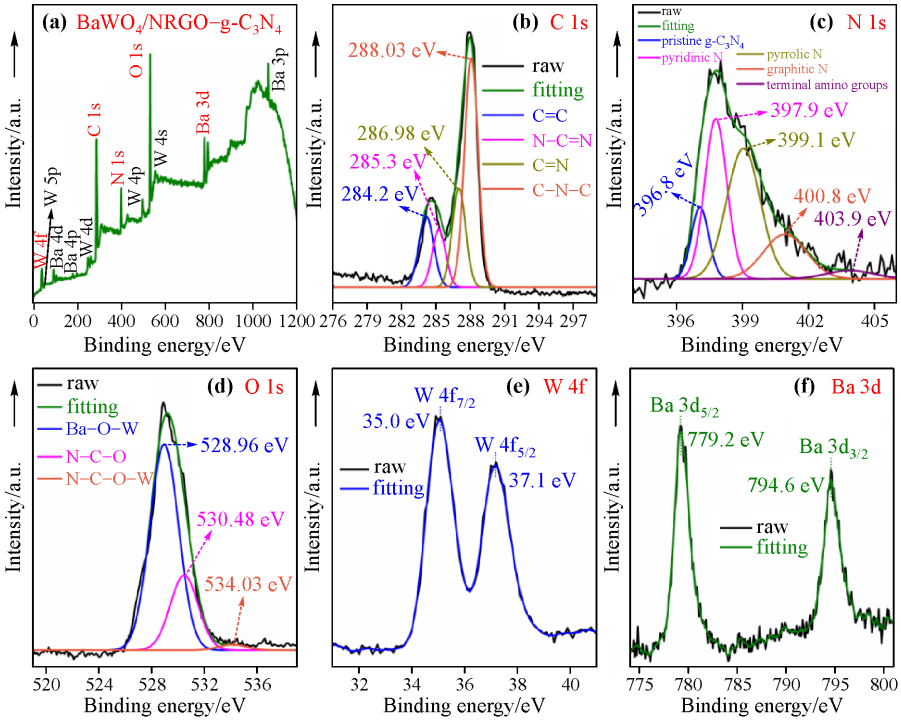

Fig. 5 XPS spectra of $BaWO_4$/NRGO–g-C_3N_4 nanocomposites: **(a)** survey; high-resolution spectra of **(b)** C 1s, **(c)** N 1s, **(d)** O 1s, **(e)** W 4f and **(f)** Ba 3d.

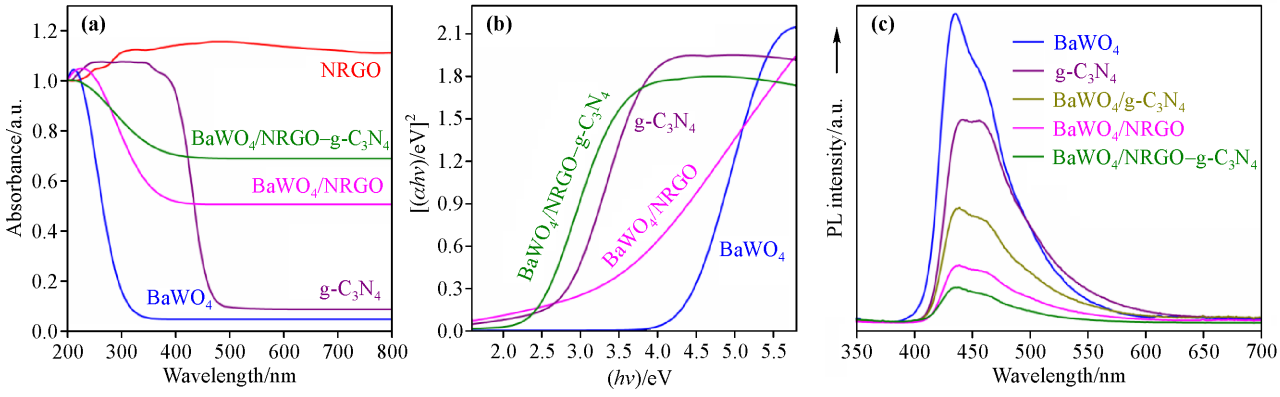

Fig. 6 **(a)** DRS spectra, **(b)** bandgap plots and **(c)** PL spectra of $BaWO_4$/NRGO–g-C_3N_4 nanocomposites.

be measured from the intercept of the tangents in the plot of $(\alpha hv)^{2/n}$ versus photon energy (hv) based on the Tauc relation given below in Eq. (2) and are shown in Fig. 6(b):

$$\alpha hv = k(hv - E_g)^{n/2} \quad (2)$$

where α, h, v and k are absorption coefficient, Planck constant, frequency of light and a constant, respectively. In addition, n is a constant determined by the type of optical transition of a semiconductor, which is equal to 1 for a direct gap material, and 4 for an indirect gap material. According to Eq. (2), the intercept of the tangents to the plots of $(\alpha hv)^2$ versus photon energy could be employed to determine the bandgaps of the given materials, due to their direct electronic transitions.

The bandgaps of pure g-C_3N_4, $BaWO_4$, $BaWO_4$/NRGO and $BaWO_4$/NRGO–g-C_3N_4 nanocomposite are 2.69, 4.43, 3.04 and 2.41 eV, respectively (Fig. 6(b)). The bandgaps of $BaWO_4$/NRGO–g-C_3N_4 nanocomposites are reduced compared to its components. The reduction in the bandgap may be attributed to the delocalization of surface charges resulted by the interactions of the components in the composite. It is believed that interactions lead to the

formation of new molecular orbitals of lower energy which in turn facilitates the reduction in the bandgap. Such observations for semiconductor composites are reported in Refs. [14,16]. Such reduction in the bandgap of the materials is beneficial for enhancing both visible-light absorption and photocatalytic activity.

3.7 PL studies

PL analysis represents the recombination performance of photogenerated charge carriers in a semiconductor. Higher rate of recombination results in higher intensity of the PL spectrum. The enhanced photocatalytic efficiency of $BaWO_4$/NRGO–g-C_3N_4 nanocomposite is attributed to the effective separation of photogenerated charge carriers [14]. The nature of charge carrier recombination in $BaWO_4$, $BaWO_4$/NRGO, $BaWO_4$/g-C_3N_4 and $BaWO_4$/NRGO–g-C_3N_4 nanocomposite was investigated by PL analysis (Fig. 6(c)). $BaWO_4$ exhibits strong emission peak around 445 nm, which is due to the recombination of the photogenerated electron–hole pairs. After NRGO or g-C_3N_4 was introduced, the heterostructure samples show lower PL emission intensity compared with that of pure $BaWO_4$, suggesting lower recombination of the photogenerated electron–hole pairs. The PL peak of $BaWO_4$/NRGO–g-C_3N_4 nanocomposite shows the lowest intensity, which reveals higher separation between the photogenerated electron–hole pairs in the $BaWO_4$/NRGO–g-C_3N_4 nanocomposite surface.

3.8 Photocatalytic studies

The nanocomposite and its components were tested for their photocatalytic activities in the degradation of MB dye. In the absence of the catalyst the degradation was negligible. As shown in Fig. 7(a), the efficiencies of pure NRGO, $BaWO_4$, g-C_3N_4, $BaWO_4$/g-C_3N_4, $BaWO_4$/NRGO, NRGO–g-C_3N_4 and $BaWO_4$/NRGO–g-C_3N_4 nanocomposites are 13.10%, 21.06%, 46.99%, 65.47%, 74.49%, 79.63% and 99.44% for 120 min visible-light irradiation, respectively. Clearly, the photocatalytic degradation efficiency of these samples decreases in the following order: $BaWO_4$/NRGO–g-C_3N_4 > NRGO–g-C_3N_4 > $BaWO_4$/NRGO > $BaWO_4$/g-C_3N_4 > g-C_3N_4 > $BaWO_4$ > NRGO. These results demonstrate that the $BaWO_4$/NRGO–g-C_3N_4 nanocomposite shows higher photocatalytic activity for MB degradation than pure NRGO, g-C_3N_4, $BaWO_4$, $BaWO_4$/g-C_3N_4, $BaWO_4$/NRGO and NRGO–g-C_3N_4.

It is observed that the kinetics of photocatalytic

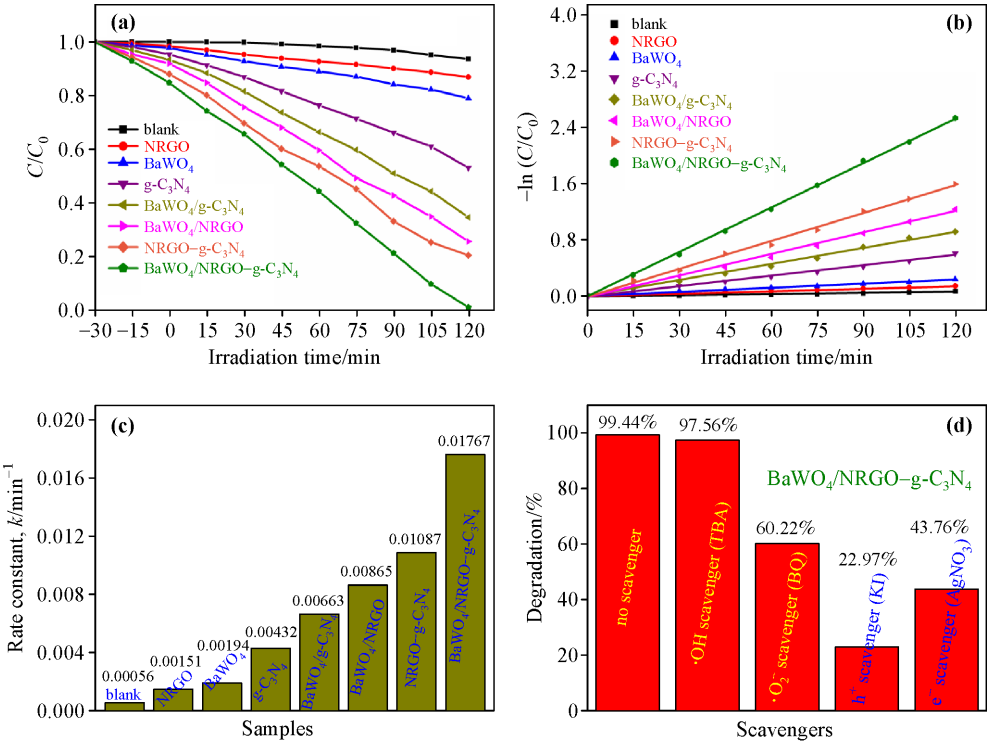

Fig. 7 **(a)** Degradation plots of MB over various catalysts, **(b)** First-order kinetics plots of MB over various catalysts, **(c)** rate constant of MB over various catalysts, and **(d)** plot depicting effects of different scavengers on degradation efficiency of $BaWO_4$/NRGO–g-C_3N_4 nanocomposites under visible-light irradiation.

degradation of MB follows the Langmuir–Hinshelwood first-order kinetics model, which can be described by the following equation:

$$-\ln\left(\frac{C}{C_0}\right) = kt \quad (3)$$

where C_0 is the initial concentration of dye, k is the first-order rate constant, C is the concentration of the dye at time interval t. The rate constants can be obtained from the slope of the plot of $-\ln(C/C_0)$ versus irradiation time (Fig. 7(b)).

The rate constant of $BaWO_4$/NRGO–g-C_3N_4 (0.01767 min^{-1}) is about 11.70, 9.11, 4.09, 2.67, 2.04 and 1.63 times greater than those of pure NRGO (0.00151 min^{-1}), $BaWO_4$ (0.00194 min^{-1}), g-C_3N_4 (0.00432 min^{-1}), $BaWO_4$/g-C_3N_4 (0.00663 min^{-1}), $BaWO_4$/NRGO (0.00865 min^{-1}) and NRGO–g-C_3N_4 (0.01087 min^{-1}), respectively (Fig. 7(c)). The enhanced performance of the ternary nanocomposite may be attributed to the factors such as narrow bandgap, higher extent of energy absorption in the visible-light region and efficient separation of charge carriers, contributing significantly towards improved photodegradation of MB in comparison to that of component materials.

The durability and stability of the photocatalysts are significantly important for their practical applications. The catalytic stability was determined by recycling the nanocomposite. The degradation rates changed from 99.44% to 99.21% to 98.82% to 98.35% to 97.44% from the 1st to the 5th cycle, respectively. These results indicate that the $BaWO_4$/NRGO–g-C_3N_4 nanocomposite is relatively stable during the photocatalytic process.

In order to understand the photocatalysis mechanism of the $BaWO_4$/NRGO–g-C_3N_4 nanocomposite, the active species generated during the photocatalytic degradation process are identified through radical and hole-trapping experiments. 10 mmol/L Ternary butyl alcohol (TBA), 10 mmol/L KI (potassium iodide), 1 mmol/L BQ (benzoquinone) and 10 mmol/L $AgNO_3$ (silver nitrate) acted as the scavengers for hydroxyl radicals (•OH), holes (h^+), superoxide radicals ($\bullet O_2^-$) and electrons (e^-), respectively.

Figure 7(d) displays the influence of different quenchers on the visible-light photocatalytic activity of $BaWO_4$/NRGO–g-C_3N_4 nanocomposite for the degradation of MB. With the addition of TBA, the photodegradation efficiency of MB did not change much indicating that the •OH is not the active species generated in the $BaWO_4$/NRGO–g-C_3N_4 photocatalytic reaction system. The degradation efficiency of MB changed slightly with the addition of BQ and $AgNO_3$, implying that $\bullet O_2^-$ and e^- were formed in the photocatalytic reaction system of $BaWO_4$/NRGO–g-C_3N_4 under the visible-light irradiation. However, after addition of KI, the photodegradation efficiency of MB decreased significantly as a result of quenching of h^+ in a reaction system, which indicated that h^+ is the main active species generated in the $BaWO_4$/NRGO–g-C_3N_4 photocatalytic degradation of MB. The proposed reactions are shown in Eqs. (4)–(7):

$$\text{g-}C_3N_4 + h\nu \rightarrow \text{g-}C_3N_4(e^- + h^+) \quad (4)$$

$$\text{g-}C_3N_4(e^-) + BaWO_4 \rightarrow \text{g-}C_3N_4 + BaWO_4(e^-) \quad (5)$$

$$BaWO_4(e^-) + O_2 \rightarrow BaWO_4 + \bullet O_2^- \quad (6)$$

$$\text{g-}C_3N_4(h^+) + \text{dye} \rightarrow CO_2 + H_2O \quad (7)$$

where e^- is the electron in the CB edge, and h^+ is the hole in the VB edge.

The visible-light photocatalytic efficiency of the $BaWO_4$/NRGO–g-C_3N_4 nanocomposite can be elucidated by the band positions of the respective semiconductor materials. Therefore, the VB and CB energy levels of $BaWO_4$ and g-C_3N_4 were measured using the Mulliken electronegativity formula:

$$E_{VB} = \chi - E_e + 0.5E_g \quad (8)$$

$$E_{CB} = E_{VB} - E_g \quad (9)$$

where, E_{VB} and E_{CB} are respectively the VB and the CB potentials; E_g is the bandgap of the semiconductor, i.e., 4.43 and 2.69 eV for $BaWO_4$ and g-C_3N_4, respectively. χ is the arithmetical mean of the absolute electronegativity of component atoms in the semiconductor, and E_e is the free electron energy based on the hydrogen scale (4.5 eV). The χ values of $BaWO_4$ and g-C_3N_4 are 5.6954 and 4.73 eV, respectively. The calculated VB potentials of $BaWO_4$ and g-C_3N_4 are 3.4104 and 1.575 eV, respectively. The CB potentials are -1.0196 and -1.115 eV, respectively, for $BaWO_4$ and g-C_3N_4.

Based on the above discussions and analysis, a possible charge transfer mechanism for the $BaWO_4$/NRGO–g-C_3N_4 nanocomposite is proposed, as shown in Fig. 8. When the system is under visible irradiation, the VB electrons of g-C_3N_4 semiconductors are excited to the CB, leaving holes in the VB, thereby forming photoinduced electron–hole pairs. Because the CB potential of $BaWO_4$ is slightly lower than that of the CB of g-C_3N_4, the CB electrons of g-C_3N_4 would easily jump to the CB of $BaWO_4$ and from there to

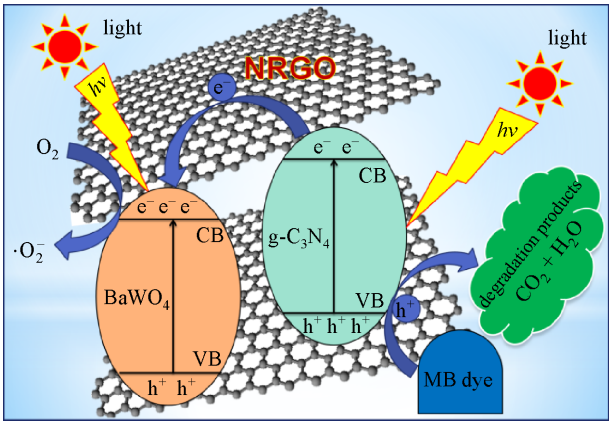

Fig. 8 The proposed mechanism for the photocatalytic degradation of dye by $BaWO_4$/NRGO–g-C_3N_4 nanocomposites under visible-light irradiation.

the highly conducting NRGO sheets, resulting in effective charge separation and transport. These electrons would then react with the oxygen to form superoxide radical anion. The holes will immediately get transported with the support of conductive NRGO matrix to react with MB to form products such as CO_2, H_2O, and other species. Thus, the entire process leads to efficient separation of the photogenerated electron–hole pairs, which in turn results in the enhancement of the photocatalytic activity of $BaWO_4$/NRGO–g-C_3N_4 nanocomposites for the degradation of MB.

In order to understand the nature of products formed during photocatalytic degradation of MB, we have determined the total organic carbon content (TOC) of the reaction medium during the photocatalysis process. Using the TOC values, percentage mineralization of the dye was calculated employing Eq. (1) given earlier. For comparison, the decrease in concentration of MB in terms of decolorization percentage was determined during the catalytic photodegradation. The concentrations of solutions were calculated from absorbance data at 664 nm. Figure 9 (a) shows absorbance versus wavelength plot at different intervals of time and Fig. 9(b) shows variations of the mineralization percentage and the decolorization percentage with time in the form of a bar diagram. As can be observed from the plot, the absorbance at 664 nm decreased with time and reached 0.56% during scan at 120 min under visible-light irradiation. The TOC value decreased to 14.36% or mineralization extent increased to 85.74% under visible-light irradiation for 120 min of visible light irradiation. Thus, the results suggest that, the organic carbon is mostly converted to CO_2 during the process. In view of this, it can be concluded that the nanocomposite is an eco-friendly photocatalyst. A comparison of photocatalytic degradation activity of reported catalysts with our catalyst is given in Table S1.

3.9 Hydrogenation studies

The catalytic activity of $BaWO_4$/NRGO–g-C_3N_4 nanocomposites was evaluated in the reduction of 4-NP using $NaBH_4$ in an aqueous solution. In the absence of the catalyst the reduction was negligible. However, when $BaWO_4$/NRGO–g-C_3N_4 nanocomposites were added into the 4-NP solution, the absorption of 4-NP found at 400 nm peak decreased immediately and the new absorption peak of 4-AP found at 300 nm was obtained, and then the intensity of this 300 nm peak increased with time as shown

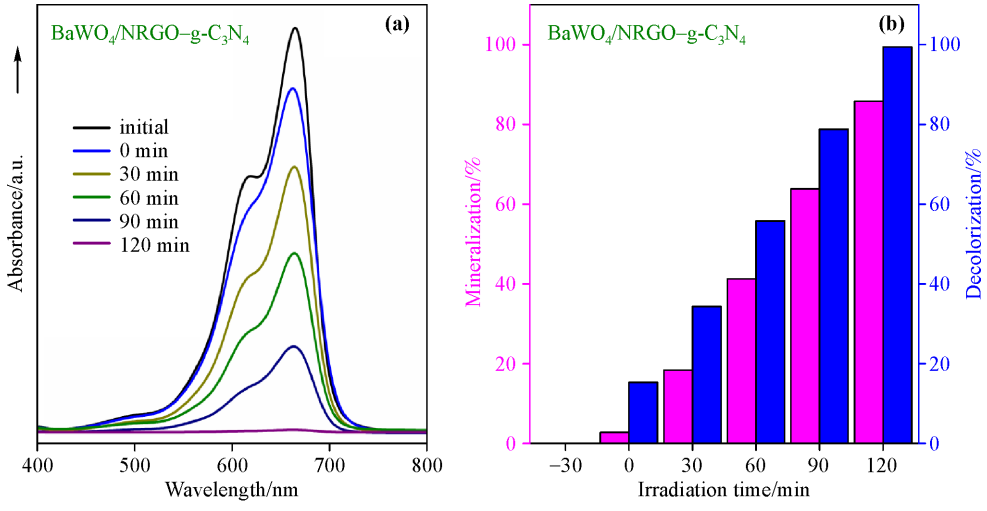

Fig. 9 **(a)** Absorbance versus wavelength and **(b)** mineralization/decolorization test bar diagram for photodegradation of MB catalyzed by $BaWO_4$/NRGO–g-C_3N_4 nanocomposites at different intervals of time.

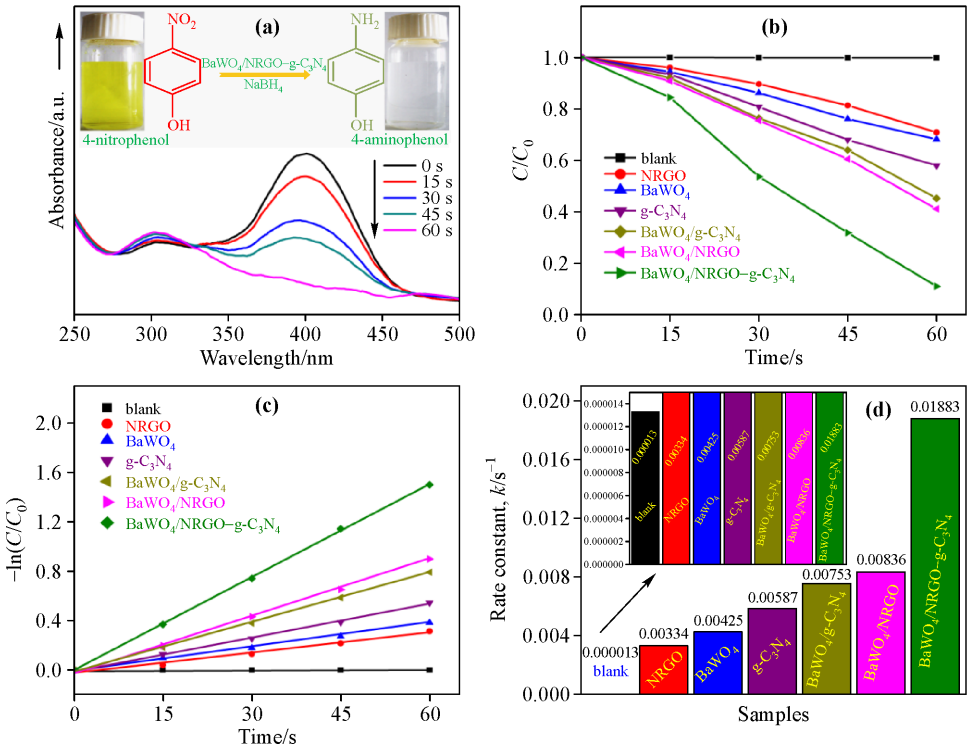

Fig. 10 **(a)** UV-vis absorption spectra for the reduction of 4-NP to 4-AP by $NaBH_4$ in the presence of $BaWO_4$/NRGO–g-C_3N_4 nanocomposites. **(b)** Catalytic reduction of 4-NP to 4-AP over various catalysts using $NaBH_4$. **(c)** First-order kinetic plots of $-\ln(C/C_0)$ against the reduction time of 4-NP to 4-AP. **(d)** Rate constant values of 4-NP over various catalytic materials.

in Fig. 10(a). The catalytic reduction of 4-NP into 4-AP was completed in 60 s. The complete change of 4-NP can be visually seen (inset of Fig. 10(a)) as the solution color changes from bright yellow to colorless. The observed results indicated that the $BaWO_4$/NRGO–g-C_3N_4 nanocomposite is an excellent catalyst in the reduction of 4-NP to 4-AP than those of pure NRGO, $BaWO_4$, g-C_3N_4, $BaWO_4$/g-C_3N_4 and $BaWO_4$/NRGO materials (Fig. 10(b)).

The reaction rate for the reduction process followed pseudo-first-order kinetics with respect to the 4-NP concentration similar to the one described for photodegradation previously. The first-order kinetic plots of $-\ln(C/C_0)$ versus conversion time for all the catalyst materials are shown in Fig. 10(c). The reaction rate constant (k) is calculated from the slope of these plots and the same is given in the form of a bar diagram for comparison as shown in Fig. 10(d). The above results clearly indicate that $BaWO_4$/NRGO–g-C_3N_4 nanocomposites exhibit a significantly enhanced catalytic activity for the reduction of 4-NP to 4-AP than that of component materials.

The catalytic stability and reusability of the $BaWO_4$/NRGO–g-C_3N_4 nanocomposites were tested after recovery from the previous reaction mixture (Fig. 11). The recycled catalyst exhibited excellent catalytic activity even after 10 successive cycles, with nearly 100% conversion within a time period of 92 s. A comparison of reduction activity of reported catalysts with our catalyst is given in Table S2.

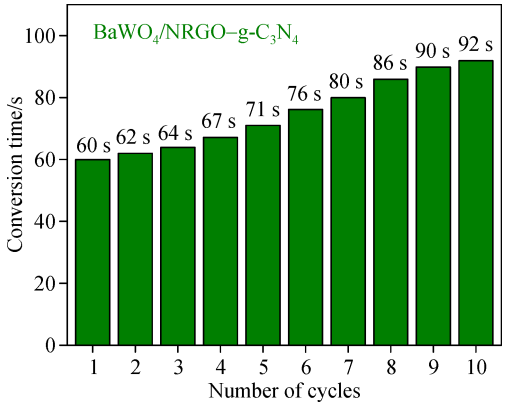

Fig. 11 Catalytic stability of $BaWO_4$/NRGO–g-C_3N_4 nanocomposites for successive 10 cycles.

3.10 Electrocatalytic studies

The electrocatalytic performance of the $BaWO_4$/NRGO–g-C_3N_4 nanocomposite was investigated in 0.1 mol/L KOH solution using a standard three-electrode system. For the

sake of comparison, component materials and 20 wt.% Pt/C were also tested under the same conditions. The polarization curves for the HER on various electrodes are shown in Fig. 12(a). $BaWO_4$/NRGO–g-C_3N_4 nanocomposites demonstrated a remarkably high activity with an onset potential of ~83 mV *vs.* RHE and a HER current density of 10 mA/cm^2 at an overpotential of 211 mV. On the other hand, $BaWO_4$/NRGO and $BaWO_4$/g-C_3N_4 had an onset potential of ~186 and ~205 mV and current density of 10 mA/cm^2 at overpotentials of 320 and 347 mV, respectively.

The linear regions of Tafel plots (Fig. 12(b)) were fitted into the Tafel equation ($\eta = b\log j + a$, where b is the Tafel slope) [28–29], yielding 30, 62, 103, 112, 160, 196 and 227 mV/dec for 20 wt.% Pt/C, $BaWO_4$/NRGO–g-C_3N_4, $BaWO_4$/NRGO, $BaWO_4$/g-C_3N_4, $BaWO_4$, NRGO and g-C_3N_4 electrodes, respectively. This indicates that the $BaWO_4$/NRGO–g-C_3N_4 nanocomposites electrode has much higher activity than the component materials electrode. Although its activity is still lower than the 20 wt.% Pt/C electrode, it may be considered significant because of the fact that it is a Pt-free catalyst. There are normally three principal steps for the HER in alkaline solutions namely, the Volmer reaction (electrochemical hydrogen adsorption: $H_2O + e^- \rightarrow H_{ads} + OH^-$), and the Tafel reaction (chemical desorption: $H_{ads} + H_{ads} \rightarrow H_2$) or the Heyrovsky process (electrochemical desorption: $H_{ads} + H_2O + e^- \rightarrow H_2 + OH^-$) [29]. Tafel slopes of 120, 40 or 30 mV/dec are expected if the Volmer, the Heyrovsky or the Tafel reactions are the rate-determining steps, respectively. Thus, the experimentally observed Tafel slope of 62 mV/dec indicated that the Heyrovsky process is the rate-determining step for $BaWO_4$/NRGO–g-C_3N_4 nanocomposites.

Stability is one of the key factors in evaluating catalyst performance. In view of this, to assess the stability of $BaWO_4$/NRGO–g-C_3N_4 nanocomposites during HER, continuous cyclic voltammograms to up to 2000 cycles, and galvanostatic polarization curves at a current density of −10 mA/cm^2 were recorded. Figure 12(c) displays LSV curves recorded at a scan rate of 10 mV/s for $BaWO_4$/NRGO–g-C_3N_4 nanocomposites before and after performing 2000 continuous cyclic voltammograms between 0.0 and −0.5 V. Notably, no appreciable activity change was observed after 2000 cycles indicating excellent stability of the $BaWO_4$/NRGO–g-C_3N_4 nanocomposites during HER. This observation further suggests that the $BaWO_4$/NRGO–g-C_3N_4 nanocomposite structure and composition remain unchanged during the catalytic process. The potential

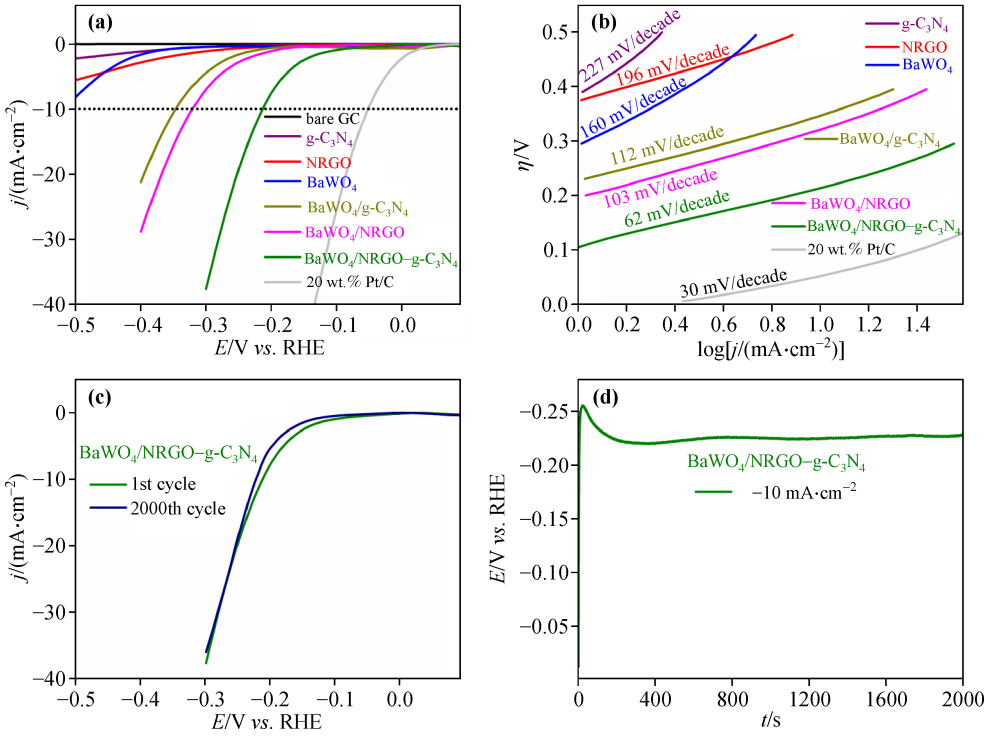

Fig. 12 **(a)** LSV and **(b)** Tafel slope curves for different electrode materials. **(c)** Stability curves and **(d)** chronopotentiometry curves at −10 mA/cm.

required to deliver a current density of -10 mA/cm^2 is an important figure of merit for the viability of a HER catalyst because it corresponds to the current density required to attain 10% efficiency in a solar-to-fuel conversion device [28–29]. Galvanostatic measurements also demonstrated the outstanding stability of the $BaWO_4$/NRGO–g-C_3N_4 nanocomposites in basic media (Fig. 12(d)), confirming that the ternary nanocomposite can be a very useful, efficient and promising candidate for HER. A comparison of electrocatalytic activity of reported catalysts with our catalyst is given in Table S1.

4 Conclusions

In this work, $BaWO_4$/NRGO–g-C_3N_4 nanocomposites were successfully synthesized by microwave irradiation method and characterized by different techniques like XRD, Raman, SEM, HRTEM, XPS, BET, PL and UV-visible spectroscopy. The synthesized composite exhibited enhanced efficiency for photodegradation of MB dye, HER, and catalytic reduction of 4-NP to 4-AP, suggesting that the material can be a very promising multifunctional catalyst. The present approach provides fundamental insights which can be extended in future to other metal tungstate-based ternary composites to act as multifunctional catalyst in the field of clean energy and environment.

Acknowledgement M.M.J.S. acknowledges the financial support from the National Institute of Technology Karnataka.

References

[1] Acar C, Dincer I, Naterer G F. Review of photocatalytic water-splitting methods for sustainable hydrogen production. International Journal of Energy Research, 2016, 40(11): 1449–1473

[2] Roger I, Shipman M A, Symes M D. Earth-abundant catalysts for electrochemical and photoelectrochemical water splitting. Nature Reviews Chemistry, 2017, 1: 0003 (14 pages)

[3] Li C, Xu Y, Tu W, et al. Metal-free photocatalysts for various applications in energy conversion and environmental purification. Green Chemistry, 2017, 19(4): 882–899

[4] Sadiq M M J, Shenoy U S, Bhat D K. High performance dual catalytic activity of novel zinc tungstate-reduced graphene oxide nanocomposites. Advanced Science, Engineering and Medicine, 2017, 9(2): 115–121

[5] Chang H, Wu H. Graphene-based nanocomposites: preparation, functionalization and energy and environmental applications. Energy & Environmental Science, 2013, 6(12): 3483–3507

[6] Sudhakar Y N, Selvakumar M, Bhat D K, et al. Reduced graphene oxide derived from used cell graphite, and its green fabrication as eco-friendly supercapacitor. RSC Advances, 2014, 4(104): 60039–60051

[7] Li X, Wang H, Robinson J T, et al. Simultaneous nitrogen doping and reduction of graphene oxide. Journal of the American Chemical Society, 2009, 131(43): 15939–15944

[8] Zhang M, Li Y, Pan D, et al. Nickel core–palladium shell nanoparticles grown on nitrogen-doped graphene with enhanced electrocatalytic performance for ethanol oxidation. RSC Advances, 2016, 6(40): 33231–33239

[9] Wu J, Shen X, Miao X, et al. An all-solid-state Z-scheme g-C_3N_4/Ag/Ag_3VO_4 photocatalyst with enhanced visible-light photocatalytic performance. European Journal of Inorganic Chemistry, 2017, (21): 2845–2853

[10] Yao J, Chen H, Jiang F, et al. Titanium dioxide and cadmium sulfide co-sensitized graphitic carbon nitride nanosheets composite photocatalysts with superior performance in phenol degradation under visible-light irradiation. Journal of Colloid and Interface Science, 2017, 490: 154–162

[11] Akhundi A, Habibi-Yangjeh A. Ternary g-C_3N_4/ZnO/AgCl nanocomposites: synergistic collaboration on visible-light-driven activity in photodegradation of an organic pollutant. Applied Surface Science, 2015, 358: 261–269

[12] Hisatomi T, Kubota J, Domen K. Recent advances in semiconductors for photocatalytic and photoelectrochemical water splitting. Chemical Society Reviews, 2014, 43(22): 7520–7535

[13] Montini T, Gombac V, Hameed A, et al. Synthesis, characterization and photocatalytic performance of transition metal tungstates. Chemical Physics Letters, 2010, 498(1–3): 113–119

[14] Zheng J Y, Haider Z, Van T K, et al. Tuning of the crystal engineering and photoelectrochemical properties of crystalline tungsten oxide for optoelectronic device applications. CrystEngComm, 2015, 17(32): 6070–6093

[15] Liu D, Huang J, Tao X, et al. One-step synthesis of C–Bi_2WO_6 crystallites with improved photo-catalytic activities under visible light irradiation. RSC Advances, 2015, 5(81): 66464–66470

[16] Sadiq M M J, Shenoy U S, Bhat D K. Novel RGO–$ZnWO_4$–Fe_3O_4 nanocomposite as high performance visible light photocatalyst. RSC Advances, 2016, 6(66): 61821–61829

[17] Sadiq M M J, Shenoy U S, Bhat D K. Enhanced photocatalytic performance of N-doped RGO–$FeWO_4$/Fe_3O_4 ternary nanocomposite in environmental applications. Materials Today Chemistry, 2017, 4: 133–141

[18] Sadiq M M J, Shenoy U S, Bhat D K. $NiWO_4$–ZnO–NRGO ternary nanocomposite as an efficient photocatalyst for degradation of methylene blue and reduction of 4-nitro phenol. Journal of Physics and Chemistry of Solids, 2017, 109: 124–133

[19] Wadhwa H, Kumar D, Mahendia S, et al. Microwave assisted

facile synthesis of reduced graphene oxide–silver (RGO–Ag) nanocomposite and their application as active SERS substrate. Materials Chemistry and Physics, 2017, 194: 274–282

[20] Yan S C, Li Z S, Zou Z G. Photodegradation performance of g-C_3N_4 fabricated by directly heating melamine. Langmuir, 2009, 25 (17): 10397–10401

[21] Zhang Y, Chen Z, Liu S, et al. Size effect induced activity enhancement and anti-photocorrosion of reduced graphene oxide/ZnO composites for degradation of organic dyes and reduction of Cr(VI) in water. Applied Catalysis B: Environmental, 2013, 140–141: 598–607

[22] Hummers W S, Offeman R E. Preparation of graphitic oxide. Journal of the American Chemical Society, 1958, 80(6): 1339

[23] Shi H, Qi L, Ma J, et al. Polymer-directed synthesis of penniform $BaWO_4$ nanostructures in reverse micelles. Journal of the American Chemical Society, 2003, 125(12): 3450–3451

[24] Zawawi S M M, Yahya R, Hassan A, et al. Structural and optical characterization of metal tungstates (MWO_4; M = Ni, Ba, Bi) synthesized by a sucrose-templated method. Chemistry Central Journal, 2013, 7(1): 80–89

[25] Clark G, Doyle W P. Infra-red spectra of anhydrous molybdates and tungstates. Spectrochimica Acta, 1966, 22(8): 1441–1447

[26] Appavu B, Kannan K, Thiripuranthagan S. Enhanced visible light photocatalytic activities of template free mesoporous nitrogen doped reduced graphene oxide/titania composite catalysts. Journal of Industrial and Engineering Chemistry, 2016, 36: 184–193

[27] Xu H, Yan J, She X, et al. Graphene-analogue carbon nitride: novel exfoliation synthesis and its application in photocatalysis and photoelectrochemical selective detection of trace amount of Cu^{2+}. Nanoscale, 2014, 6(3): 1406–1415

[28] Subramanya B, Bhat D K, Shenoy U S, et al. Novel Fe–Ni–graphene composite electrode for hydrogen production. International Journal of Hydrogen Energy, 2015, 40(33): 10453–10462

[29] Subramanya B, Ullal Y, Shenoy U S, et al. Novel Co–Ni–graphene composite electrodes for hydrogen production. RSC Advances, 2015, 5(59): 47398–47407

Supplementary information

Table S1 Comparison of the photocatalytic degradation process parameters for reported catalysts

Photocatalyst	Light source	Concentration	Degradation extent, Time	Refs.
g-C_3N_4–NS/$CuCr_2O_4$ (10%)	visible light (50 W LED lamp)	catalyst: 0.1 g RhB: 250 mL (2.5×10^{-5} mol/L)	98.8%, 210 min	[S1]
g-C_3N_4/TiO_2	visible-light (350 W xenon arc lamp, cutoff filter, 420 nm)	catalyst: 0.04 g (20 mL) RhB: 30 mL (1×10^{-5} mol/L)	95.2%, 90 min	[S2]
rGO–TiO_2–0.55CdS	visible light (300 W Xe lamp, cutoff filter, 400 nm)	catalyst: 5 mg MB: 80 mL (5 mg/L) or 4-CP: 25 mL (1 mg/L)	90.3% (MB) and 65.3% (40-CP), 60 min	[S3]
AgCl@Ag/N-rGO	light source (150 W Xe arc lamp, cutoff filter, 400 nm)	catalyst: 1.6 g/L 2-CP: 60 mL (10 mg/L)	97%, 150 min	[S4]
RGO/Ag/TiO_2-nanotubes/Ti plates	UV resource (125 W mercury lamp)	MB: 100 mL (10 ppm)	89%, 120 min	[S5]
Cu-doped TiO_2/RGO	UV light source (UV-A light 300 W, λ = 315–400 nm)	MB: 35 mL (10 ppm)	63%, 180 min	[S6]
Graphene–Bi_2MoO_6	visible light (250 W halogen lamp, cutoff filter, 400 nm)	brilliant red X-3B (25 mg/L) 0.1 g of photocatalyst (200 mL)	90.4%, 90 min	[S7]
$BaWO_4$/NRGO–g-C_3N_4	visible-light source (250 W mercury lamp, cutoff filter, 400 nm)	catalyst: 20 mg MB: 200 mL (20 mg/L)	99.44%, 120 min	this work

Table S2 Comparison of 4-NP to 4-AP reduction parameters of reported catalysts

Catalyst	Time	Rate constant	Refs.
Pd–GA/RGO	5 min	0.1199 min^{-1}	[S8]
[Pt(ppy)Cl(3-ampy)]/GO	840 s	2.04×10^{-3} s^{-1}	[S9]
AgNPs@MWCNTs–polymer composite	5 min	0.473 min^{-1}	[S10]
Pd/RGO/Fe_3O_4	60 min	3.06 min^{-1}	[S11]
Ni–RGO	480 s	1.8×10^{-3} s^{-1}	[S12]
GO/Ag	30 s	14.5×10^{-3} s^{-1}	[S13]
$BaWO_4$/NRGO–g-C_3N_4	60 s	0.1883 s^{-1}	this work

Table S3 Comparison of HER parameters using alkaline medium for reported catalysts

Catalyst	*U*/mV *vs.* RHE at −10 mA·cm^{-2}		Tafel slope/(mV·dec^{-1})	Refs.
	Onset potential	Over potential		
Mo_2C@NPC	−137	–	126.4	[S14]
MoS_2 CNTs aerogel	−210	–	135	[S15]
Carbon paper/carbon tubes/cobalt-sulfide	–	190	138	[S16]
AuNPs@NCNRs/CNFs-8	−190	386	110	[S17]
CoO_x@N-doped carbon	–	232	115	[S18]
Fe@N–C	–	330	158	[S19]
N, P-doped graphene	389	585	145	[S20]
$BaWO_4$/NRGO–g-C_3N_4	83	211	62	this work

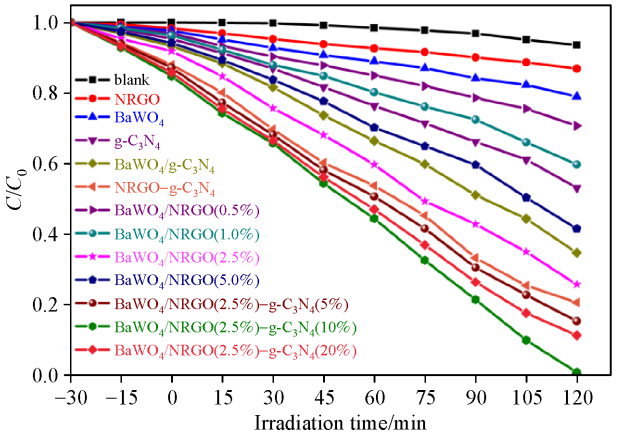

Fig. S1 Catalytic activities of various compositions of $BaWO_4$/NRGO–g-C_3N_4 nanocomposites.

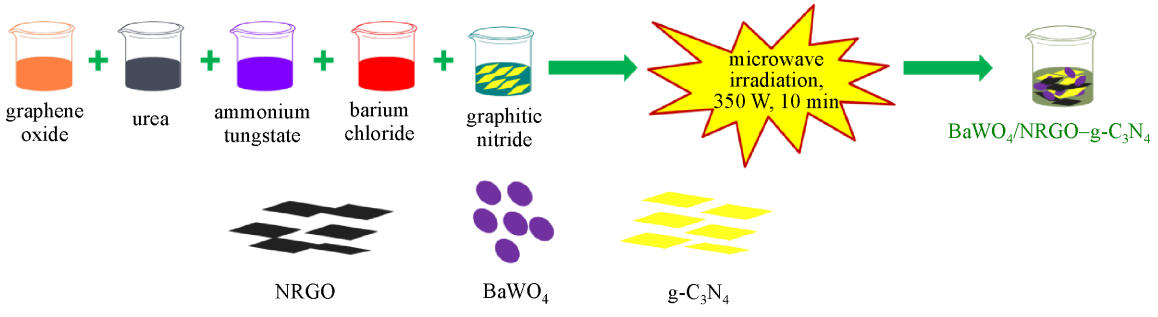

Fig. S2 Schematic representation of the synthesis of $BaWO_4$/NRGO–g-C_3N_4 ternary nanocomposites.

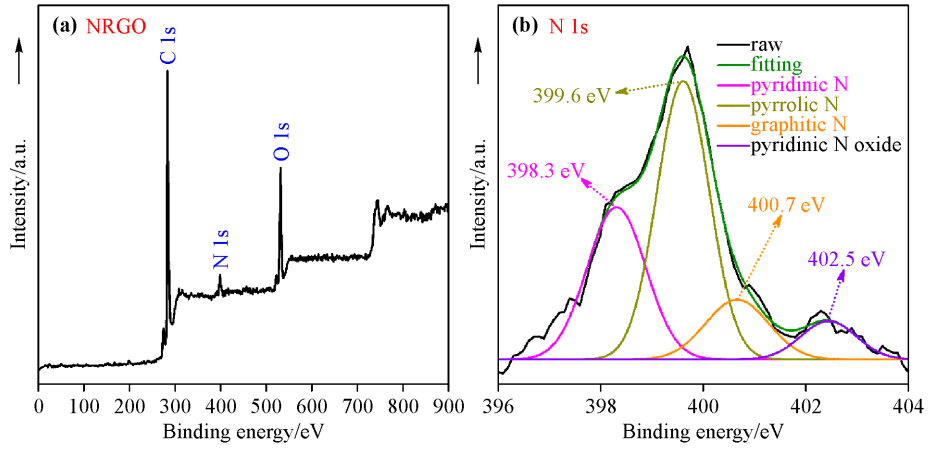

Fig. S3 **(a)** Survey and **(b)** high resolution of N 1s spectra of NRGO.

References

[S1] Akhundi A, Habibi-Yangjeh A. Graphitic carbon nitride nanosheets decorated with $CuCr_2O_4$ nanoparticles: Novel photocatalysts with high performances in visible light degradation of water pollutants. Journal of Colloid and Interface Science, 2017, 504: 697–710

[S2] Hao R, Wang G, Jiang C, et al. *In situ* hydrothermal synthesis of g-C_3N_4/TiO_2 heterojunction photocatalysts with high specific surface area for rhodamine B degradation. Applied Surface Science, 2017, 411: 400–410

[S3] Tian Z, Yu N, Cheng Y, et al. Hydrothermal synthesis of graphene/TiO_2/CdS nanocomposites as efficient visible-light driven photocatalysts. Materials Letters, 2017, 194: 172–175

[S4] Wang L, Shi Y, Wang T, et al. Silver chloride enwrapped silver grafted on nitrogen-doped reduced graphene oxide as a highly efficient visible-light-driven photocatalyst. Journal of Colloid and Interface Science, 2017, 505: 421–429

[S5] Faraji M, Mohaghegh N. Ag/TiO_2-nanotube plates coated with reduced graphene oxide as photocatalysts. Surface and Coatings Technology, 2016, 288: 144–150

[S6] Pham T T, Nguyen-Huy C, Lee H J, et al. Cu-doped TiO_2/reduced graphene oxide thin-film photocatalysts: Effect of Cu content upon methylene blue removal in water. Ceramics International, 2015, 41(9): 11184–11193

[S7] Wang P, Ao Y, Wang C, et al. A one-pot method for the preparation of graphene–Bi_2MoO_6 hybrid photocatalysts that are responsive to visible-light and have excellent photocatalytic activity in the degradation of organic pollutants. Carbon, 2012, 50(14): 5256–5264

[S8] Vilian A T E, Choe S R, Giribabu K, et al. Pd nanospheres decorated reduced graphene oxide with multi-functions: Highly efficient catalytic reduction and ultrasensitive sensing of hazardous 4-nitrophenol pollutant. Journal of Hazardous Materials, 2017, 333: 54–62

[S9] Fath R H, Hoseini S J, Khozestan H G. A nanohybrid of organoplatinum(II) complex and graphene oxide as catalyst for reduction of p-nitrophenol. Journal of Organometallic Chemistry, 2017, 842: 1–8

[S10] Alshehri S M, Almuqati T, Almuqati N, et al. Chitosan based polymer matrix with silver nanoparticles decorated multiwalled carbon nanotubes for catalytic reduction of 4-nitrophenol. Carbohydrate Polymers, 2016, 151: 135–143

[S11] Atarod M, Nasrollahzadeh M, Sajadi S M. Green synthesis of Pd/RGO/Fe_3O_4 nanocomposite using *Withania coagulans* leaf extract and its application as magnetically separable and reusable catalyst for the reduction of 4-nitrophenol. Journal of Colloid and Interface Science, 2016, 465: 249–258

[S12] Tian Y, Liu Y, Pang F, et al. Green synthesis of nanostructed Ni-reduced graphene oxide hybrids and their application for catalytic reduction of 4-nitrophenol. Colloids and Surfaces A: Physicochemical and Engineering Aspects, 2015, 464: 96–103

[S13] Mao A, Zhang D, Jin X, et al. Synthesis of graphene oxide sheets decorated by silver nanoparticles in organic phase and their catalytic activity. Journal of Physics and Chemistry of Solids, 2012, 73(8): 982–986

[S14] Wu Z Y, Hu B C, Wu P, et al. Mo_2C nanoparticles embedded within bacterial cellulose-derived 3D N-doped carbon nanofiber networks for efficient hydrogen evolution. NPG Asia Materials, 2016, 8(7): e288

[S15] Reddy S, Du R, Kang L, et al. Three dimensional CNTs aerogel/MoS_x as an electrocatalyst for hydrogen evolution reaction. Applied Catalysis B: Environmental, 2016, 194: 16–21

[S16] Wang J, Zhong H X, Wang Z L, et al. Integrated three-dimensional carbon paper/carbon tubes/cobalt-sulfide sheets as an efficient electrode for overall water splitting. ACS Nano, 2016, 10(2): 2342–2348

[S17] Zhang M, Wang S, Li T, et al. Nitrogen and gold nanoparticles Co-doped carbon nanofiber hierarchical structures for efficient hydrogen evolution reactions. Electrochimica Acta, 2016, 208: 1–9

[S18] Jin H, Wang J, Su D, et al. *In situ* cobalt–cobalt oxide/N-doped carbon hybrids as superior bifunctional electrocatalysts for hydrogen and oxygen evolution. Journal of the American Chemical Society, 2015, 137(7): 2688–2694

[S19] Wang J, Gao D, Wang G, et al. Cobalt nanoparticles encapsulated in nitrogen-doped carbon as a bifunctional catalyst for water electrolysis. Journal of Materials Chemistry A: Materials for Energy and Sustainability, 2014, 2(47): 20067–20074

[S20] Zheng Y, Jiao Y, Li L H, et al. Toward design of synergistically active carbon-based catalysts for electrocatalytic hydrogen evolution. ACS Nano, 2014, 8(5): 5290–5296